Desalination and Water Treatment
www.deswater.com

doi: 10.5004/dwt.2022.28407

256 (2022) 314–327
April

Degradation of Acid Orange II by sludge-derived biochar supported Cu/Fe bimetallic particles activating persulfate

Yan Wang*, Teng Jiang, Xingjun Fan, Haiming Zou, Jianrong Zhao

Department of Environmental Science and Engineering, Anhui Science and Technology University, Donghua Road 9#, Fengyang 233100, China, emails: wangyanht@163.com (Y. Wang), 406154738@qq.com (T. Jiang), 934151553@qq.com (X. Fan), 1517228169@qq.com (H. Zou), 653124657@qq.com (J. Zhao)

Received 19 August 2021; Accepted 17 March 2022

ABSTRACT

$CuFe_2O_4$ and biochar composite (CuFe/BC) was successfully prepared by a simple hydrothermal synthesis method. As an excellent catalyst, it was utilized toward the activation of persulfate (PS) for Acid Orange II (AOII) degradation. The surface morphology and structure characterizations of CuFe/BC measured by X-ray diffraction, scanning electron microscopy-energy-dispersive X-ray spectroscopy, Fourier-transform infrared spectroscopy, X-ray photoelectron spectroscopy, and Brunauer–Emmett–Teller. The CuFe/BC exhibited high catalytic activity and reusability. The AOII degradation rate could reach 0.106 min^{-1} and AOII degradation efficiency was 95.89%. After 4 reuse cycle, CuFe/BC exhibited good reactivity in CuFe/BC/PS system and AOII degradation efficiency still kept 73.58%. During the AOII degradation process in CuFe/BC/PS system, the main active radicals ($SO_4^{\bullet-}$, $^{\bullet}OH$, and $^1O_2$) were identified by the radical scavenging experiment and electron spin resonance analysis. Moreover, the mechanism of the CuFe/BC/PS system for AOII degradation was further proposed. The acute toxicity of the reaction solution to *Photobacterium phosphoreum* T3 spp. in the CuFe/BC/PS process increased during the first 20 min and then decreased, which illustrated that CuFe/BC/PS was an effective and safe method for the removal of AOII.

Keywords: Acute toxicity; Acid Orange II degradation; $CuFe_2O_4$ and biochar composite; Degradation mechanism; Persulfate

1. Introduction

Widespread use of dyes for the paper, textile, cosmetics, drugs, food, leather, plastic and rubber industries has led to ubiquitous contamination of soil surface and water resources, resulting in serious environmental problems [1–5]. More than 70% of the available dyes on the market today were azo dyes characterized by the presence of nitrogen-to-nitrogen double bonds (–N=N–) [6]. Acid Orange II (AOII), as a representative azo dye, is of high stability and powerful resistance to biodegradation in aerobic conditions, resulting in a great challenge for the degradation [6,7]. Therefore, an efficient technique to eliminate AOII from wastewater is required urgently.

Advanced oxidation processes (AOPs) based on sulfate radicals ($SO_4^{\bullet-}$, SR-AOPs) have been extensively employed as the effective way for the removal of organic pollutants [6,8]. $SO_4^{\bullet-}$ is mostly generated thereby activation of persulfate (PS) by using heat [8,9], alkaline [10], transition metals [11], ultraviolet light (UV) [12,13], microwave [14], electron conduction and electrochemical [15], minerals and metal oxides [4,6,16–18], photochemical [16], gamma ray [15], ultrasonic irradiation [19], semiconductors [20], carbonaceous-based materials [9,15,17,20,21], and so on.

Among these activation methods, the heterogeneous catalytic process had been widely employed for dye wastewater treatment due to its low cost, energy-saving route and easy operation [16,22]. The development of heterogeneous

* Corresponding author.

catalysts was the key of the heterogeneous catalytic process. The use of nanoparticles during the heterogeneous catalytic process was evenly enhanced compared with the traditional catalyst systems. $CuFe_2O_4$, one of spinel ferrite, has been proved as an effective catalyst for the activation of PS to degrade organic pollutants [10,23], such as, 4-chlorophenol [24], p-nitrophenol [25], metoprolol [26], trimethoprim [27], ofloxaci [22], and acetaminophen [28]. However, the particulate aggregation of $CuFe_2O_4$ due to its magnetic nature limited the population of active sites and reduced its catalytic activity [27]. The loading of $CuFe_2O_4$ onto suitable supporting materials, such as carbon materials not only overcome the aggregation of $CuFe_2O_4$ nanoparticles, but also increased active sites [27,29,30]. Biochar (BC) has unique properties, including large surface area and large mechanical strength, which make BC suitable to be the supporting materials for catalyst loading [30–33]. Moreover, BC could activate PS to generate $SO_4^{\bullet-}$ due to the oxygen functional groups on BC surface such as carboxyl, hydroxyl and carbonyl [30,34,35]. Fe functionalized biochar, as the catalyst for the activation of PMS, showed an excellent efficiency for bisphenol A (BPA) degradation [36]. The BC-supported nanoscale zero-valent iron catalysts was successfully prepared by Luo et al. [37] and was used in PS activation for the synergistic degradation of aromatic pollutants in alkaline wastewater. But the CuFe/BC/PS system has not been employed for AOII degradation.

In this study, $CuFe_2O_4$ and biochar composite (CuFe/BC) were synthesized with hydrothermal method and coupled with PS to degrade AOII in aqueous solution. This study has the following purposes: (i) CuFe/BC is expected to be efficient in the catalytic activation of PS at room temperature, (ii) the removal mechanism of AOII in the CuFe/BC/PS system and the reusability of the CuFe/BC composite are investigated, (iii) Moreover, the effects of other key factors like catalyst dosage, PS concentration, and solution pH on the degradation rate are also investigated.

2. Materials and methods

2.1. Chemicals

AOII (≥85%) was purchased from Aladdin Chemistry Co., Ltd., (Shanghai, China). Sodium peroxydisulfate ($Na_2S_2O_8$, PS, ≥98%), copper(II) chloride dihydrate ($CuCl_2{\cdot}2H_2O$, ≥99%), ferric chloride ($FeCl_3$, ≥97%), sodium borohydride ($NaBH_4$, ≥98%), sodium azide (NaN_3), ethyl alcohol (EtOH, ≥75%) and *tert*-butanol (TBA, ≥99%) were purchased from the Sinopharm Chemical Reagent Co., Ltd., (Shanghai, China). 5,5-dimethyl-1-pyrroline N-oxide (DMPO) and 4-oxo-2,2,6,6-tetramethylpiperidine (TEMP) were purchased from Aladdin Industrial Corporation (Shanghai, China). All solutions were freshly prepared before each run in deionized water.

2.2. Preparation of BC and CuFe/BC

For sludge-derived biochar (BC) preparation, the municipal sewage sludge was obtained from sludge dewatering room in Fengyang Sewage Treatment Plant. After being dried at 80°C, smashed and sifted through 80 mesh sieves, the sludge powders were pyrolyzed in a tubular reactor (SK-G04123K, China) and the pyrolysis temperature was set at 500°C for 2 h.

CuFe/BC were synthesized via a hydrothermal synthesis according to the previous study [38,39]. 1 g BC was firstly added into 80 mL deionized water and completely dispersed through an ultrasonic method. Then $CuCl_2{\cdot}2H_2O$ (10 mmol) and $FeCl_3$ (20 mmol) were added into the above suspension and were dissolved by stirring vigorously. Following this treatment, 1 g NaOH was added into the above mixture solution with continual stirring for 10 min. The resulting mixture was transferred to a 100 mL Teflon-lined stainless steel autoclave and put in an oven at 180°C for 24 h. The obtained precipitates were washed for several times with excessive deionized water and ethanol. Finally, the CuFe/BC catalyst was obtained by drying at 60°C for 12 h. In addition, the $CuFe_2O_4$ was prepared by the similar procedure without BC.

2.3. Experimental procedure

The catalytic degradation experiments were performed in 250 mL batch reactors at 25°C ± 2°C by water batch heating. The 200 mL AOII solution was added into batch reactors, and the initial pH of the solution was adjusted by using Mettler Toledo FE20 pH Meter (Mettler Toledo FE20, Shanghai) with 0.1 mmol/L H_2SO_4 or NaOH. Then a prespecified amount of PS and catalyst were added to initiate the reaction and mixed by a magnetic stirrer at a rotary speed of 150 rpm (IKA color squid white, Germany). At prespecified time intervals, 4 mL aqueous sample was taken and filtered through 0.22 μm filter. Then the AOII concentration was measured by a UV-Visible spectrophotometer (UV-1750, Shimadzu, Japan) at the detection wavelength of 484 nm and the total organic carbon (TOC) values of the samples were measured by a TOC analyzer (TOC-L, Shimadzu, Japan). The TOC removal was calculated by using Eq. (1):

$$\text{TOC removal}(\%) = \left(1 - \frac{\text{TOC}_t}{\text{TOC}_0}\right) \times 100 \quad (1)$$

where TOC_0 and TOC_t are the initial and residual TOC concentration of sample at 0 and t min, respectively.

The AOII catalytic degradation reactions described above were repeated for four cycles to evaluate the recyclability of CuFe/BC catalyst. After each catalytic run, the catalyst was separated by vacuum filtration, and washed with ultrapure water several times, then dried at 60°C overnight for reuse test to study its longevity.

In addition, in order to determine the role of radical species formed in the catalytic system, a series of quenching tests were carried out by using TBA, NaN_3 and EtOH as the radical scavengers, respectively. All experiments were conducted in triplicate, and the error bars represented standard deviation of the means.

2.4. Analytical methods

The morphology of catalysts was characterized by a scanning electron microscopy (SEM) and an energy-dispersive

X-ray spectroscopy (EDS) analysis (Hitachi S-3000N, Japan). The X-ray diffraction (XRD) spectra of the catalyst including CuFe/BC, $CuFe_2O_4$ and BC were collected on X-ray diffractometer (Bruker D8 ADVANCE, Germany) with Cu Kα radiation (λ = 1.5406 Å) by scanning the sample from 10° to 80° at the scan rate of 5°min^{-1} operating under 40 kV and 30 mA. The surface chemical state was measured by X-ray photoelectron spectroscopy (XPS, Thermo Fisher, USA) using an ESCALAB 250Xi photoelectron spectrometer with monochromatic Al Kα radiation.

The Fourier-transform infrared spectrometer (FTIR, Nicolet Avatar 330) was employed to determine surface functional groups of BC, $CuFe_2O_4$, synthesized CuFe/BC, and used CuFe/BC through the infrared spectra in the range of 400–4,000 cm^{-1}. Zeta potential (ZP) of samples was measured with a zeta voltmeter (Brookhaven ZetaPALS, USA). Specific surface area and pore volume were examined using a surface area and pore size analyzer (JW-BK132F, China) with Brunauer–Emmett–Teller (BET) theories.

The formation of active radicals were identified with electron spin resonance (ESR) on Bruker A300-10/12 (Germany) with a microwave bridge (receiver gain, 1 × 10^5, modulation amplitude, 2 G, microwave power, 20 mW, modulation frequency, 100 kHz).

2.5. Microtox acute toxicity assay

The active toxicities of AOII mixture samples were determined with the luminescent bacteria based on water quality-determination of the acute toxicity-luminescent bacteria test (GB/T 15441-1995). The freeze-dried powder of *Photobacterium phosphoreum* T3 spp. was purchased from the Institute of Soil Science, Chinese Academy of Sciences (Nanjing, China). The *Photobacterium phosphoreum* T3 spp. can radiate a certain intensity of visible light with a wavelength of 50–490 nm when being reconstituted by 3% NaCl [40]. The variation of luminescence from *Photobacterium phosphoreum* T3 spp was detected using a Toxicity Determinator (DXY-3, Institute of Soil Science, Chinese Academy of Sciences, Nanjing, China). In the blank test, the effluent of AOII degradation was replaced deionized water. The toxicity was characterized by the percentage of inhibiting luminosity (R) by Eq. (2)

$$R(\%) = \left(1 - \frac{\text{Luminosity of the sample}}{\text{Luminosity of the CK}}\right) \times 100 \quad (2)$$

where CK is blank sample. To ensure data accuracy, the toxicity was measured by three replicates for each effluent sample. The samples were filtered through 0.22 μm filter before test.

3. Results and discussion

3.1. Characterization of catalysts

The SEM micrographs of BC, $CuFe_2O_4$, and CuFe/BC, and EDS pattern of CuFe/BC are shown in Fig. 1. As shown in Fig. 1a and b, compared with plate-like structure of BC, the $CuFe_2O_4$ clusters consisted of microparticles. It is clear from Fig. 1c that the surface morphology of CuFe/BC was basically the same with BC (Fig. 1a) and it maintained the original morphology of BC and plate-like structure were seen clearly, besides tiny $CuFe_2O_4$ granules attached to the external surface of BC. EDS analysis of the stochastic zone in Fig. 1c was used to investigate the chemical composition of CuFe/BC surface and the atomic ratio of Cu to Fe was nearly equal to 1:4 (Fig. 1d), which was not consistent with the molecular formula of $CuFe_2O_4$. It also proved that BC doped with other iron oxides, such as Fe_2O_3. The similar phenomenon was reported by Liu et al. [41].

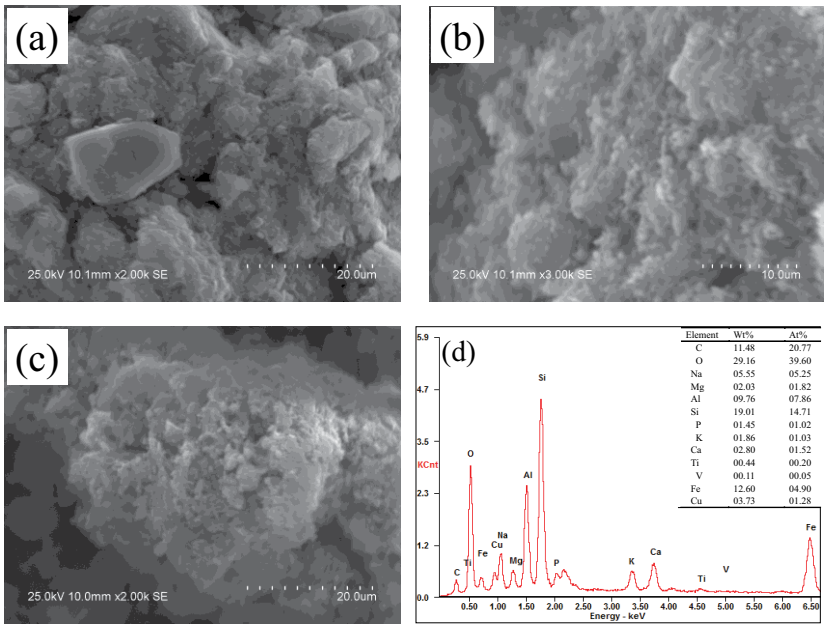

Fig. 1. SEM image of (a) BC, (b) $CuFe_2O_4$, (c) CuFe/BC and (d) EDS of CuFe/BC.

To further understand the load composition of BC, the phase components of BC, $CuFe_2O_4$, and synthesized CuFe/BC were characterized by XRD. As can be seen in Fig. 2a, both BC and CuFe/BC displayed a carbon characteristic diffraction peak at 2θ of 26° [27], which proved that their carbon skeletons were not destroyed during the synthesis. The diffraction peaks for CuFe/BC were similar to the standard diffraction data for $CuFe_2O_4$ (JCPDS 34-0425) [42,43] and Fe_2O_3 (JCPDS 24-0081) [44]. The diffraction peaks at 2θ = 18.3°, 29.9°, 34.7°, 35.9°, 37.1°, 43.8°, 57.8°, and 62.2° could be ascribed to the (101), (112), (103), (211), (202), (220), (321) and (224) reflections of tetragonal $CuFe_2O_4$, and the peaks at 2θ = 30.2°, 35.6°, 43.3°, 57.3° and 62.9° are indexed to the (220), (311), (400), (511) and (440) reflections of the γ-Fe_2O_3 phase. The diffraction peaks of CuFe/BC were wider than that of bare $CuFe_2O_4$ due to $CuFe_2O_4$ particle aggregation.

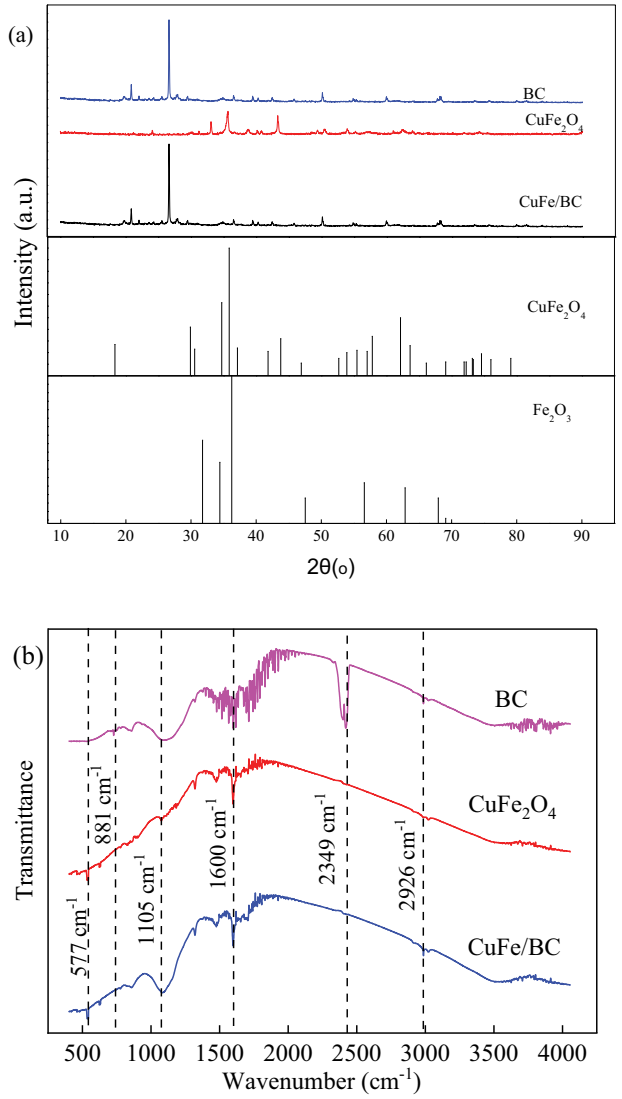

Fig. 2. (a) XRD patterns and (b) FTIR spectra of BC, $CuFe_2O_4$, and CuFe/BC.

The BET surface area, total pore volume, micropore volume and average pore diameter of the derived BC, $CuFe_2O_4$ and CuFe/BC were presented in Table S1. The BET surface area, total pore volume and micropore volume of CuFe/BC were 93.93 m^2/g, 132.98 mL/g, and 35.95 mL/g, respectively, which were larger than that of BC. The presence of $CuFe_2O_4$ in CuFe/BC increased the BET surface area, total pore volume and micropore volume due to the much larger BET surface area, total pore volume and micropore volume of $CuFe_2O_4$ compared with BC. But the average pore diameter of CuFe/BC was 5.66 nm, which decreased compared with BC. Because the average pore diameter of $CuFe_2O_4$ was smaller than that of BC.

It has been reported that BC, as a carbonaceous material, is a promising environmental remediation material due to the rich oxygen-functional groups on its surface and high surface areas [45]. In order to determine the characterization of BC, $CuFe_2O_4$, and CuFe/BC, the FTIR was employed and the result was shown in Fig. 2b. As expected in FTIR spectra (Fig. 2b), the peaks at 881; 1,105; 1,600 and 2,926 cm^{-1} in both of BC and CuFe/BC were assigned to aromatic C–H, C–O stretching vibrations, the stretching vibration of C=O or C=C and long linear aliphatic chain –CH_2 groups [27,30,46], indicating the presence of these characteristic groups remained in a hydrothermal system. The band at 2,349 cm^{-1} in BC represented CO_2 asymmetric stretching vibrations, which indicated that BC absorbed CO_2 from the air [46]. Interestingly, compared with the FTIR spectra of BC, the band at 2,349 cm^{-1} disappeared and the band at 577 cm^{-1} appeared in that of CuFe/BC. The band at 577 cm^{-1} in FTIR spectra of $CuFe_2O_4$ and CuFe/BC justified metal-O stretching mode [47].

XPS was employed to evaluate the chemical characterization and surface chemical state of CuFe/BC, and the result was shown in Fig. 3a. As can be seen from Fig. 3a, atomic ratio of C, O, Fe and Cu elements in CuFe/BC were 19.55%, 69.53%, 8.65% and 2.27%, respectively. The atomic ratio of Fe and Cu elements was approximately 4 and bigger than 2. It illustrated that iron oxides presented in CuFe/BC composite since the atomic ratio of Fe and Cu elements in $CuFe_2O_4$ was 2. These results are similar to those of EDS. The regional C 1s, O 1s, Fe 2p and Cu 2p XPS spectra of CuFe/BC are displayed in Fig. 3b–e. Four peaks of C 1s at 284.80, 285.80, 287.20, and 292.20 eV are observed in Fig. 3b, which were assigned to the sp2 graphitic carbon C–C, C–OH, C=O, and π–π*, respectively [48,49]. The O 1s XPS spectra in Fig. 3c are resolved in to two peaks centered at 530.3 and 531.2 eV, which represented metal oxide bond (M–O, M: Cu or Fe) and C=O bonds, respectively [48,50]. According to previous reports [51–54] and the Cu 2p spectrum (Fig. 3d), the peaks centered at 934.32 eV for Cu $2p_{3/2}$ and 953.76 eV for Cu $2p_{1/2}$ suggested the existence of Cu(II) in CuFe/BC and their vibrating satellites at 941.57 and 961.76 eV illustrated Cu^{2+} ions [51,52]. Another peak at 933.14 eV was attributed to Cu^+ on the surface of CuFe/BC [52]. Fig. 3e displays the Fe 2p XPS spectra of CuFe/BC and the peak at around 724.25 eV could be assigned to Fe $2p_{1/2}$ when other one at around 711.13 eV could be correspond to Fe $2p_{3/2}$ [54]. The fitted curve of Fe $2p_{3/2}$ could be de-convoluted into three peaks. The peak located at 709.2 corresponds to

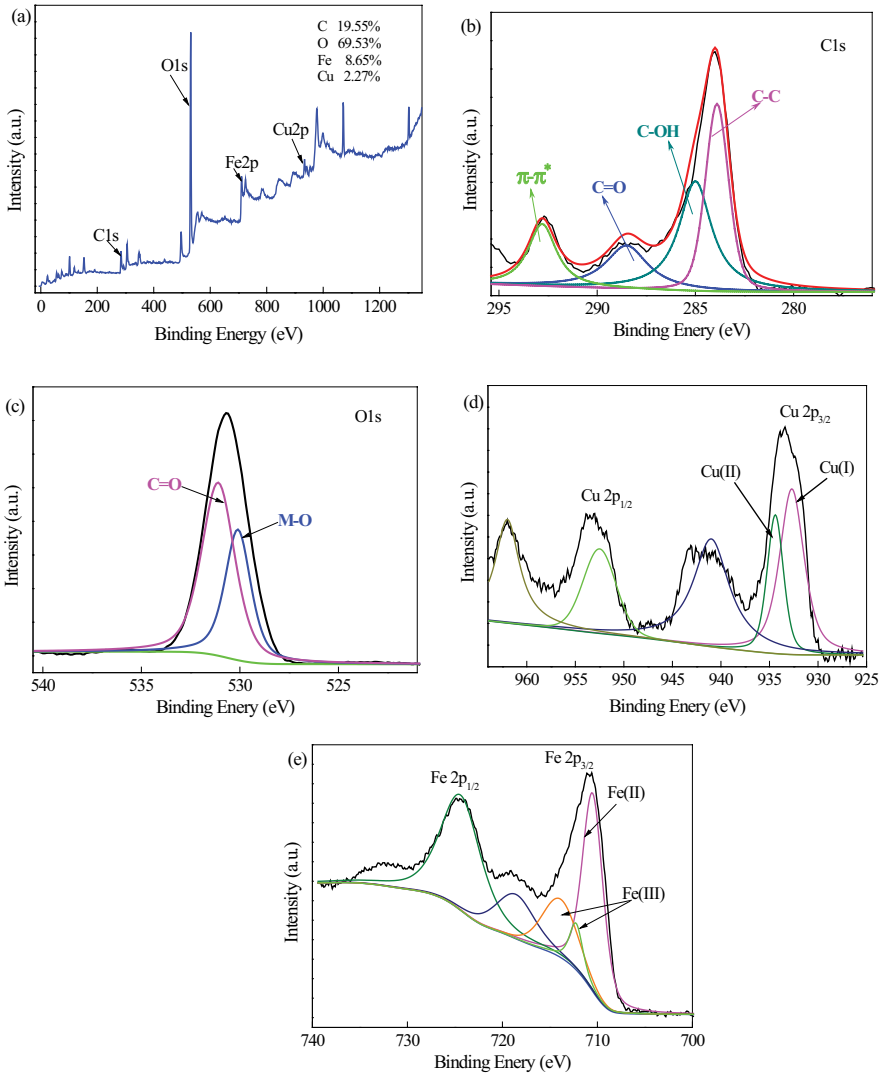

Fig. 3. XPS spectra of (a) whole XPS spectra of CuFe/BC and typical elements (b) C 1s, (c) O 1s, (d) Fe 2p and (e) Cu 2p.

Fe(II) when the peaks at 710.81 and 712.14 eV indicate Fe(III) [52,54]. Moreover, the 712.14 eV also is the standard spectrum of Fe–O–Cu, representing the existence of $CuFe_2O_4$ [54].

3.2. Catalytic performance

To demonstrate the remarkable ability of the CuFe/BC/PS system, the degradation experiments were carried out with BC alone, CuFe/BC alone, PS alone Fe_2O_3 alone, $CuFe_2O_4$ alone, BC/PS, Fe_2O_3/PS, $CuFe_2O_4$ and CuFe/BC with PS for 90 min. The result is shown in Fig. 4 and the pseudo-first-order model was evaluated to simulate AOII elimination as described in Eq. (3):

$$\frac{dC}{dt} = -k_1 C \tag{3}$$

where C (mg/L) represents the AOII concentration at reaction time t (min), and k_1 (min^{-1}) represents the pseudo-first-order rate constant of AOII removal. As shown in Fig. 4b and Table S2, the plot data of AOII removal in BC/PS, Fe_2O_3/PS, $CuFe_2O_4$/PS, and CuFe/BC systems were well fitted to the pseudo-first-order kinetics model, which was verified by the very high correlation coefficients R^2 ranged from 0.930 to 0.998.

From Fig. 4a, it can be illustrated that the Fe_2O_3 alone, PS alone, and $CuFe_2O_4$ alone exhibited negligible degradation ratio of AOII, while the adsorption of BC, $CuFe_2O_4$, and CuFe/BC for AOII were almost less than 10%. However, the addition of PS greatly improved the AOII degradation ratio. The AOII removal ratio in BC/PS was 51.43% with the reaction rate constants of 0.013 min^{-1}, which illustrated that PS could be activated by BC to produce active species. It can be associated with the oxygen-containing functional groups (C–OH, C=O and –COOH) on the surface of BC, which could activate PS to produce $SO_4^{\bullet-}$ as shown in Eqs. (4)–(5) [48,55,56]. Moreover, C=O on the surface of BC could promote PS self-decomposition and electron-transfer to generate $^1O_2$ [12,18,57–59].

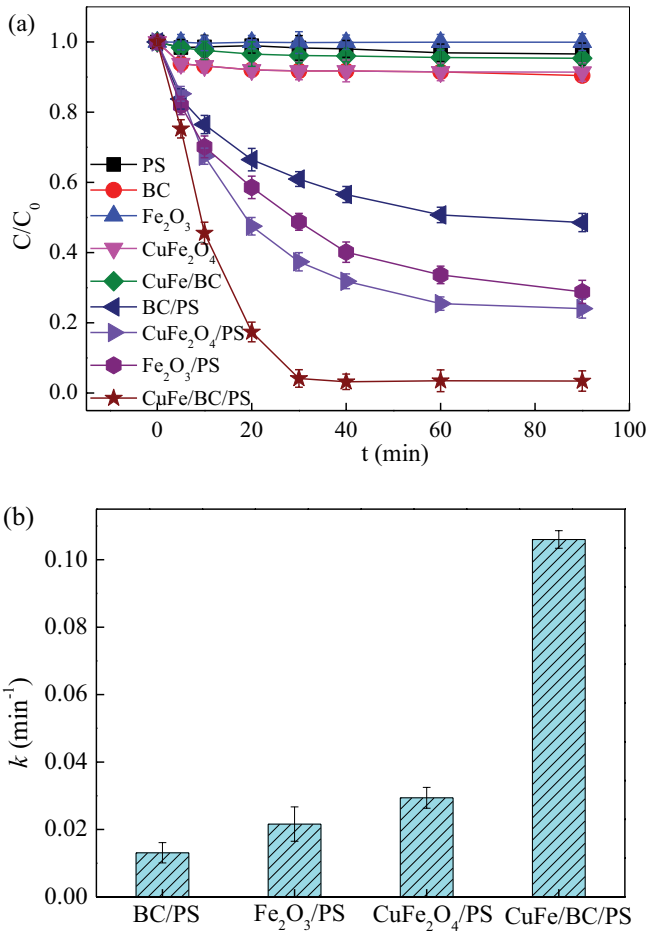

Fig. 4. Decolorization efficiency of AOII in different system (a, b) (C_0 = 50 mg/L, pH = 6, PS = 10 mmol/L, BC = 1 g/L, Fe_2O_3 = 0.7 g/L, $CuFe_2O_4$ = 0.7 g/L, CuFe/BC = 1 g/L).

$$BC{\equiv}OOH + S_2O_8^{2-} \rightarrow SO_4^{\bullet -} + HSO_4^- + BC{\equiv}OO^{\bullet} \quad (4)$$

$$BC{\equiv}OH + S_2O_8^{2-} \rightarrow SO_4^{\bullet -} + HSO_4^- + BC{\equiv}O^{\bullet} \quad (5)$$

In Fe_2O_3/PS and $CuFe_2O_4$/PS system, the AOII removal reached 71.19% and 75.95% with the reaction rate constants of 0.022 and 0.029 min^{-1}, respectively. It illustrated that PS could be activated by Fe_2O_3 and $CuFe_2O_4$ to produce active species [52]. Compared with Fe_2O_3 and $CuFe_2O_4$, CuFe/BC exhibited satisfactory catalytic activities for PS and the AOII removal reached 95.79% with the reaction rate constants of 0.106 min^{-1}, which suggested that CuFe/BC catalyst could be a promising candidate for the AOII removal.

In order to further proved the catalytic degradation reactions of AOII in CuFe/BC/PS system, the synergistic effect between Fe_2O_3, $CuFe_2O_4$ and PS was evaluated based on the synergy factor (SF) as described in Eq. (6) [12,18]:

$$SF = \frac{\text{AOII removal rate}\left(min^{-1}\right)\text{ in CuFe/BC/PS}}{\text{AOII removal rate}\left(min^{-1}\right)\text{in}\left(BC/PS + CuFe_2O_4/PS + Fe_2O_3/PS\right)} \quad (6)$$

Considering Eq. (6) and Table S2, the value of SF was found to be 1.66 for the AOII degradation in CuFe/BC/PS system, indicating the synergistic effect for this system [12]. Clearly, BC provided a suitable carrier for Fe_2O_3 and $CuFe_2O_4$, which prevented the particulate aggregation of Fe_2O_3 or $CuFe_2O_4$ and improved their catalytic performance.

3.3. Effects of catalyst dosage, PS addition, pH, and coexistent anion

The following experiments were conducted to study the effect of CuFe/BC addition on the AOII degradation in the CuFe/BC/PS system when pH = 6, the initial concentration of AOII (C_0) was 50 mg/L, and the initial concentration of PS was 10 mmol/L. As shown in Fig. 5a, when the dosage of CuFe/BC increased from 0.5 to 1 g/L, the AOII degradation efficiency increased from 76.88% to 95.89%, and the degradation rate increased from 0.018 to 0.106 min^{-1} (Table S2). Obviously, the AOII degradation was mainly dependent on the active sites on the surface of CuFe/BC, the AOII degradation efficiency was enhanced with the increasing dosage of CuFe/BC due to more active sites by the increasing catalysts for free radical generation from PS [60]. Therefore, the degradation rate of AOII increased with the increasing CuFe/BC addition. However, the degradation rate and the degradation efficiency were nearly the same when the dosage of CuFe/BC increased to 1.2 g/L. Because the free radical came from the decomposition of PS and the totality of free radicals was very constant when the PS addition was fixed.

Initial PS concentration among 4–12 mmol/L with a controlled condition (CuFe/BC loading was 1 g/L, pH = 6, the initial concentration of AOII was 50 mg/L) was explored for AOII removal and the result is shown in Fig. 5b and Table S2. The AOII degradation rate improved approximately from 0.044 to 0.106 min^{-1} with the increasing PS concentration among 4 to 10 mmol/L. It was attributed to the fact that PS was the source of radicals in the CuFe/BC/PS system and the increment of PS concentration was conducive to the catalytic oxidation, consequently accelerating the AOII degradation rate. Then, the AOII degradation rate kept nearly invariable when the PS concentration further increased to 12 mmol/L. This phenomenon may be caused by the constant active sites on the surface of CuFe/BC, which limited the activation speed of PS and the AOII degradation rate.

As is known to all, the values of zero charge point on the surface of the catalyst and solution pH played an important role in the generation of free radicals and degradation of pollutants. Nevertheless, the zeta potentials of CuFe/BC at varying pH were measured, from which the pH of point of zero charge (pH_{PZC}) was calculated to be 6.24 (Fig. S1). Meanwhile, it is necessary to evaluate the effect of solution pH on the AOII degradation. The AOII degradation performance was investigated at different pH when CuFe/BC addition was 1 g/L, the initial concentration of AOII was 50 mg/L, and the initial PS concentration was 10 mmol/L. As can be seen in Fig. 5c and Table S2, the AOII degradation rate reached maximum (0.106 min^{-1}) when the initial pH was 6 closed to pH_{PZC}. Interestingly, the similar degradation rates (about 0.098 min^{-1}) were obtained when pH

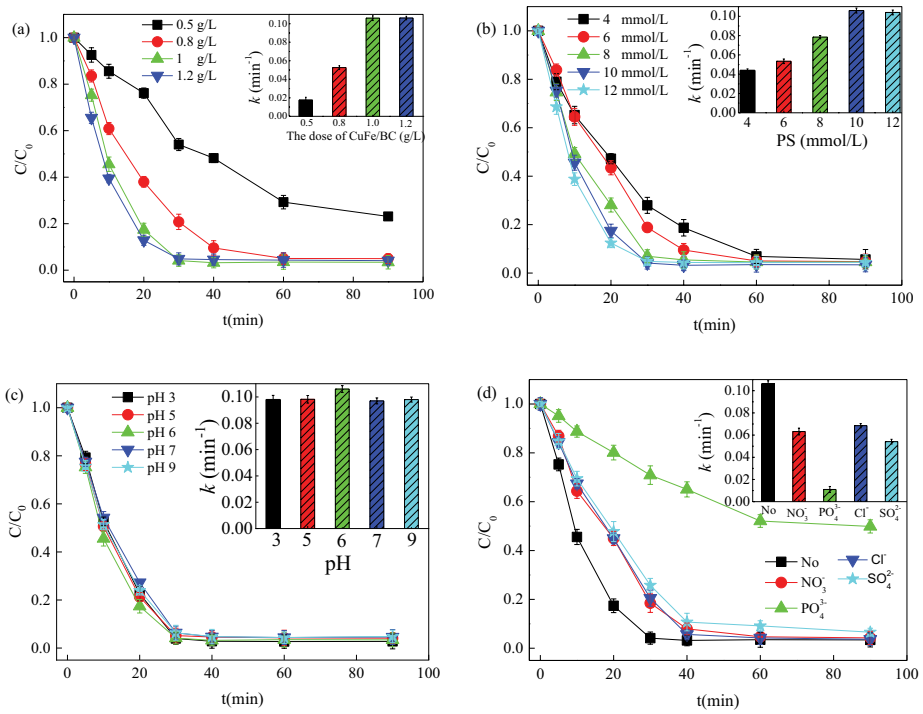

Fig. 5. Effect of reaction conditions for the decolorization of AOII: (a) catalyst dosage, (b) PS concentration, (c) initial pH, and (d) anion (C_0 = 50 mg/L, pH = 6, PS = 10 mmol/L, CuFe/BC = 1 g/L, inorganic anions = 10 mmol/L).

changed from 3 to 9. It is due to the fact that CuFe/BC has high catalytic activity and owns a wide pH range. Moreover, the surface charge of CuFe/BC was little impact on the AOII degradation rate. The result indicated that the system was suitable for a relatively wide range of pH and was consistent with the past study reported by Wang et al. [61].

Different coexisting inorganic anions in actual water bodies could react with active species came from PS activation, and then produced an important effect on the degradation efficiency of organic pollutants [62,63]. Therefore, the effect of 10 mmol/L inorganic anions (Cl^-, NO_3^-, SO_4^{2-} and PO_4^{3-}) on the AOII degradation was evaluated when CuFe/BC addition was 1 g/L, pH = 6, the initial concentration of AOII was 50 mg/L, and the initial concentration of PS was 10 mmol/L and the result is revealed in Fig. 5d. Compared with the CuFe/BC/PS system, AOII degradation efficiencies exhibited no significant change in presence of 10 mmol/L Cl^-, NO_3^-, or SO_4^{2-} after 90 min reaction and AOII degradation rate decreased. However, the presence of PO_4^{3-} inhibited obviously the oxidation activity of the CuFe/BC/PS system. The decrease could be attributed to the fact that inorganic anions would react with the active species (such as $SO_4^{\bullet-}$ and $^{\bullet}OH$) and generate new reactive radical with slower oxidation capacity [63–65], ultimately reduce the AOII degradation rate and the AOII degradation efficiency.

3.4. Reusability of CuFe/BC

The potential reusability of catalyst is a key characteristic. Further experiments were conducted to evaluate the reusability of CuFe/BC on AOII degradation and the result

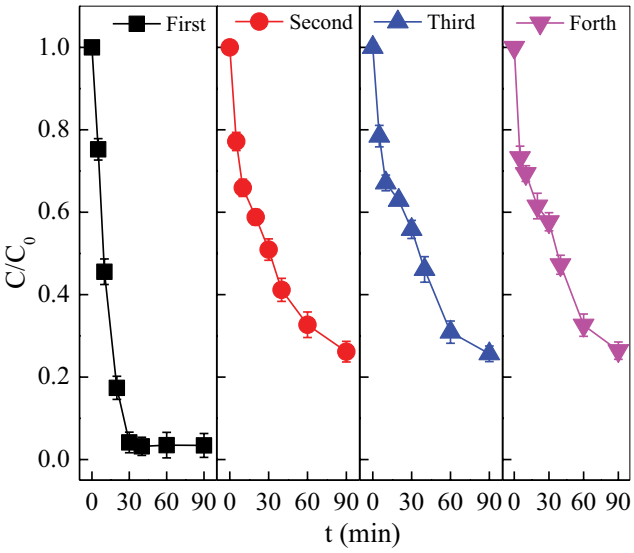

Fig. 6. Reusability of the CuFe/BC catalyst (C_0 = 50 mg/L, pH = 6, PS = 10 mmol/L, CuFe/BC = 1 g/L).

is shown in Fig. 6. It can be seen from Fig. 6 that the AOII degradation efficiencies in the four times were 95.79%, 73.83%, 74.35%, and 73.58%, respectively. Compared with the first use of CuFe/BC, the AOII degradation rates for the next three times were decreased. The reusability and the adsorption of BC were investigated when BC addition was 1 g/L, pH = 6, the initial concentration of AOII was 50 mg/L, and the initial PS concentration was 10 mmol/L and the result is shown in Fig. S2. The adsorption of AOII

by used BC compared with fresh BC did not decrease significantly, indicating that the decrease of the AOII degradation rates for the next three times could not be explain fully by the adsorption of BC. But the AOII degradation rate decreased from 54.27% (in fresh BC/PS system) to 18.19% (in used BC/PS system), indicating that the decline of catalytic performance of BC played a contribution significantly to the decline of the AOII degradation efficiency in the CuFe/BC/PS system. Because most of oxygen functional groups of BC surface (such as –COOH or –OH) were consumed for the first use to active PS or electron transfer [56,59]. However, it can be seen in Fig. S3 that the change of the functional groups of the supporter (BC) did not impact significantly on the structure of CuFe/BC. In addition, the stability of the metal on CuFe/BC was determined by dissolution test at pH 3–9 and negligible iron and copper was examined in the solution, illustrating that CuFe/BC remained the satisfactory stability and reusability.

3.5. Identification of reactive radical species and catalytic mechanism

ESR (with DMPO and TEMP as the trapping agent) was conducted to identify free radicals generated from PS, BC/PS and CuFe/BC/PS system. As shown in Fig. 7a, the obvious characteristic peaks of DMPO-OH (a relative intensity of 1:2:2:1, $\alpha_N = \alpha_H = 14.9$ G) and DMPO-SO_4 (a six-line signal of 1:1:1:1:1:1, $\alpha_N = 1.58$ G, $\alpha_H = 2.58$ G) adducts were successfully observed in BC/PS and CuFe/BC/PS system, confirming the existence of $^{\bullet}OH$ and $SO_4^{\bullet-}$ [66–68]. But they were absent in alone PS system. Meanwhile, the noticeable signals of TEMP-$^1O_2$ were also identified and are shown in Fig. 7b, proving the presence of $^1O_2$ in BC/PS and CuFe/BC/PS system [69,70]. Finally, both free radical and non-free radical oxidation were included in the AOII degradation process by BC/PS and CuFe/BC/PS.

To shed light on the contribution of the active species for AOII degradation, three free radical quenchers (TBA, EtOH and NaN_3) were added in CuFe/BC/PS system. TBA was used as mainly specific $^{\bullet}OH$ quencher due to the rate constants ((3.0–3.9) × 10^9 M/s) while it was a weak quencher for $SO_4^{\bullet-}$ ($k_{SO_4^{\bullet-}} = 4 \times 10^5$ M/s) [71,72]. EtOH was the universal quencher for $^{\bullet}OH$ and $SO_4^{\bullet-}$ ($k_{SO_4^{\bullet-}} = (1.6–7.7) \times 10^7$ M/s, $k_{^{\bullet}OH} = (1.2–2.8) \times 10^9$ M/s) [71] when NaN_3 was used as the $^1O_2$ scavenger ($k_{^{\bullet}OH} = 1.2 \times 10^7$ M/s) [70]. As shown in Fig. 8, the degradation efficiencies of AOII in presence of TBA, EtOH, NaN_3, and no quencher were 89.44%, 67.97%, 91.58% and 95.79%, respectively. The addition of TBA quenched $^{\bullet}OH$ to consequently remove AOII and the removal rate was reduced by 6.35%, while the addition of EtOH quenched both $^{\bullet}OH$ and $SO_4^{\bullet-}$ and reduced the overall efficiency of AOII degradation by 27.82%, suggesting $SO_4^{\bullet-}$ contributed to about 21.37% and $SO_4^{\bullet-}$ played the more importer role in AOII degradation compared with $^{\bullet}OH$. The result indicated that $^1O_2$ was produced in the CuFe/BC/PS system and had effect on the degradation efficiencies of AOII.

The presence of $^{\bullet}OH$, $SO_4^{\bullet-}$ and $^1O_2$ could be confirmed by radical scavenging tests and ESR analysis, which illustrated that AOII degradation included the radical pathway and non-radical pathway. According to the results above, the possible mechanisms of catalytic oxidation of AOII by

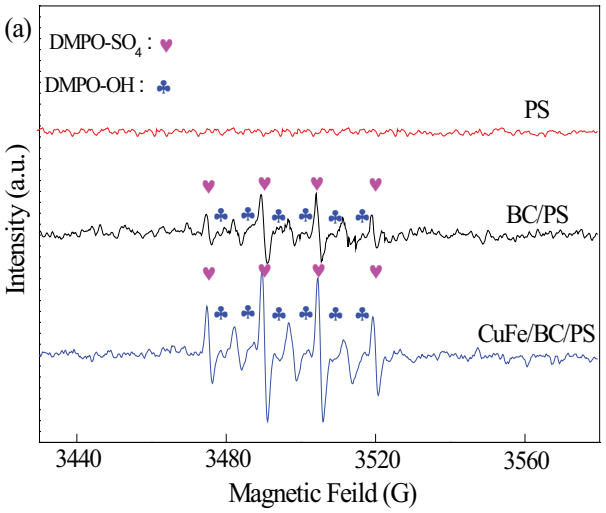

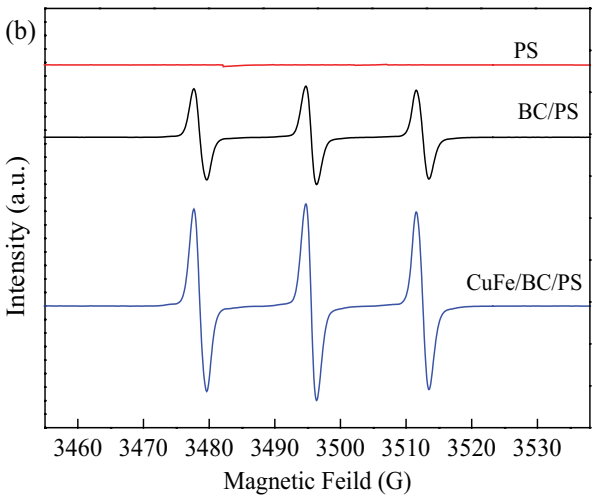

Fig. 7. ESR spectra of (a) DMPO-$^{\bullet}OH$ and DMPO-$SO_4^{\bullet-}$, (b) TEMP-$^1O_2$ signals in PS, BC/PS, and CuFe/BC/PS system (C_{DMPO} = 10 mg/L, C_{TEMP} = 10 mg/L, pH = 6, PS = 10 mmol/L, CuFe/BC = 1 g/L, BC = 1 g/L).

CuFe/BC activated PS are proposed as follows in Eqs. (4)–(5), (7)–(17) and shown in Fig. S4. For the radical-degradation pathway, PS in solution was adsorbed on the surface of CuFe/BC and catalytically activated by CuFe/BC to yield radicals [52,58,68,73]. PS could react with $\equiv Cu^{2+}$ to produce $\equiv Cu^{3+}$ and $SO_4^{\bullet-}$ (Eq.(7)). Then, hydrolysis of $SO_4^{\bullet-}$ could generate $^{\bullet}OH$ through Eq. (8). Meanwhile, PS could hydrolyze to produce HSO_5^- under acidic conditions [Eq. (9)]. Due to the unstable state of $\equiv Cu^{3+}$ in CuFe/BC composite, it was difficult to identify by XRD and XPS. $\equiv Cu^{3+}$ would quickly react with H_2O or HSO_5^- to regenerate Cu^{2+} and $^{\bullet}OH$ or $SO_5^{\bullet-}$ through Eqs. (10) and (11). Interestingly, $\equiv Cu^{2+}$ could react with HSO_5^-, resulting in the generation of $\equiv Cu^+$ and $SO_5^{\bullet-}$ by Eq. (12). Apart from these, $\equiv Fe^{3+}$ could be reduced to $\equiv Fe^{2+}$ while $\equiv Cu^{2+}$ regeneration could be realized [Eq. (13)]. Meanwhile, $\equiv Fe^{2+}$ also could active HSO_5^- to produce $SO_5^{\bullet-}$,

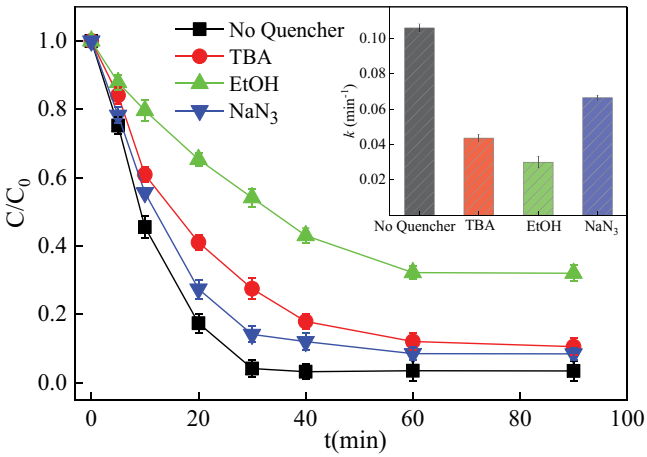

Fig. 8. Effect of radical scavengers on the decolorization of AOII (C_0 = 50 mg/L, pH = 6, PS = 10 mmol/L, CuFe/BC = 1 g/L, C_{TBA} = 5 mmol/L, C_{EtOH} = 5 mmol/L, C_{NaN_3} = 5 mmol/L).

and regenerate ≡Fe^{3+} by Eq. (14). As the supporter, BC also could decompose PS to generate $SO_4^{\bullet-}$ through the electron-transfer due to oxygen functional groups of BC surface, such as –COOH or –OH [58,59].

Besides, non-free radicals in AOII degradation process also played an important role through Eqs. (15)–(17). Fe^{2+} reacted with O_2 and simultaneously produced $O_2^{\bullet-}$ as shown in Eq. (15) [57]. Then, $O_2^{\bullet-}$ under acidic conditions was transformed to $^1O_2$ [Eq. (16)] [70]. In addition, C=O on CuFe/BC surface could activate PS to generate $^1O_2$ [Eq. (17)] [57,73,74].

$$\equiv Cu^{2+} + S_2O_8^{2-} \rightarrow \equiv Cu^{3+} + SO_4^{\bullet-} + SO_4^{2-} \quad (7)$$

$$SO_4^{\bullet-} + H_2O \rightarrow SO_4^{2-} + {}^{\bullet}OH + H^+ \quad (8)$$

$$S_2O_8^{2-} + H_2O \rightarrow HSO_5^- + HSO_4^- \quad (9)$$

$$\equiv Cu^{3+} + HSO_5^- \rightarrow \equiv Cu^{2+} + SO_5^{\bullet-} + H^+ \quad (10)$$

$$\equiv Cu^{3+} + H_2O \rightarrow \equiv Cu^{2+} + {}^{\bullet}OH + H^+ \quad (11)$$

$$\equiv Cu^{2+} + HSO_5^- \rightarrow \equiv Cu^{+} + SO_5^{\bullet-} + H^+ \quad (12)$$

$$\equiv Fe^{3+} + \equiv Cu^{+} \rightarrow \equiv Fe^{2+} + \equiv Cu^{2+} \quad (13)$$

$$\equiv Fe^{2+} + HSO_5^- \rightarrow \equiv Fe^{3+} + SO_5^{\bullet-} + H^+ \quad (14)$$

$$\equiv Fe^{2+} + O_2 \rightarrow \equiv Fe^{3+} + O_2^{\bullet-} \quad (15)$$

$$O_2^{\bullet-} + 2H^+ \rightarrow {}^1O_2 + H_2O_2 \quad (16)$$

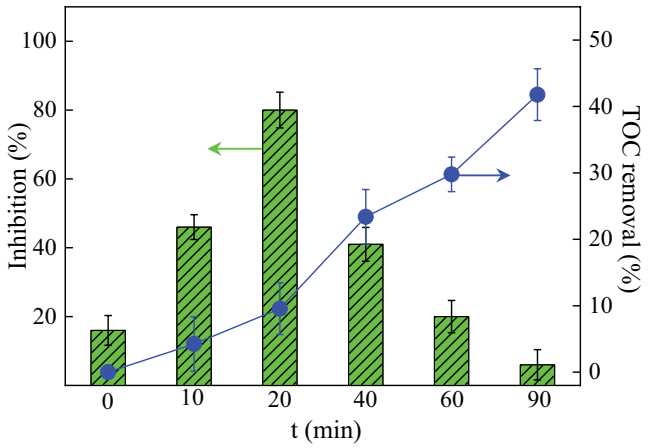

Fig. 9. Changes of acute toxicity and TOC removal during AOII degradation process (C_0 = 50 mg/L, pH = 6, PS = 10 mmol/L, CuFe/BC = 1 g/L).

$$S_2O_8^{2-} + 4OH^- \rightarrow {}^1O_2 + 2H_2O + 2SO_4^{2-} \quad (17)$$

3.6. Toxicity assessment and mineralization of effluent

As we all know, the degradation of organic pollutants did not mean that it was mineralized completely to small molecular substances such as CO_2 and H_2O. Thus, the mineralization of AOII was monitored through the TOC change of AOII effluent and the result is shown in Fig. 9. It can be seen that the TOC removal was only 41.78% after 90 min treatment, illustrating most intermediates did not be mineralized.

The variation of the acute toxicity of AOII mixture samples was monitored by the inhibition on the intensity of luminescence from *Photobacterium phosphoreum* T3 spp. As shown in Fig. 9, the inhibition of luminescence by AOII degradation effluent firstly increased and reached maximum (about 80%) after 20 min treatment, indicating the more toxic intermediate-products were produced at the early stage of the oxidation. Then, the inhibition gradually dropped to 6% at 90 min. The similar results were reported by Liu et al. [1] and Yu et al. [75]. These results indicated that highly toxic intermediates could be further degraded into harmless products.

4. Conclusions

A novel bimetallic carbonaceous catalyst with $CuFe_2O_4$ and Fe_2O_3 was successfully synthesized and demonstrated the high catalytic activity and reusability for remediation of dye wastewater. AOII degradation rate was promoted by higher initial PS concentration, higher CuFe/BC addition, but was inhibited by Cl^-, NO_3^-, SO_4^{2-} and PO_4^{3-}. AOII degradation rate kept high in a wide range of pH. Both the free radicals ($^{\bullet}OH$, and $SO_4^{\bullet-}$) and non-free radical ($^1O_2$) existed in the CuFe/BC/PS system and participated in AOII degradation. In addition, the acute toxicity of the effluent during AOII degradation process firstly increased to 80% after 20 min reaction, and then gradually decreased to 6%. In sum, CuFe/BC is an effective catalyst for PS activation towards the remediation of dye wastewater.

Acknowledgments

This study was supported by the Natural Science Foundation of Anhui Province (No. 1808085MB49, 2008085ME169, 2108085MD140), in China; Major science and technology projects in Anhui Province (18030701214), National innovation and entrepreneurship training program for College Students (201810879087).

References

[1] F. Liu, P. Yi, X. Wang, H. Gao, H. Zhang, Degradation of Acid Orange 7 by an ultrasound/ZnO-GAC/persulfate process, Sep. Purif. Technol., 194 (2018) 181–187.
[2] F. Rehman, M. Sayed, J.A. Khan, N.S. Shah, H.M. Khan, D.D. Dionysiou, Oxidative removal of brilliant green by UV/$S_2O_8^{2-}$, UV/HSO_5^- and UV/H_2O_2 processes in aqueous media: a comparative study, J. Hazard. Mater., 357 (2018) 506–514.
[3] P. Verma, S.K. Samanta, Microwave-enhanced advanced oxidation processes for the degradation of dyes in water, Environ. Chem. Lett., 16 (2018) 969–1007.
[4] M. Jose, K. Sriram, R. Reshma, U.V. Vidya, S. Shukla, Synergistic persulfate activation as an efficient and cost-effective approach for removal of organic synthetic-dyes from aqueous solutions using magnetic Pd-Fe_3O_4-flyash composite particles as catalyst, J. Environ. Chem. Eng., 6 (2018) 3709–3717.
[5] S. Karimifard, M.R. Alavi Moghaddam, Application of response surface methodology in physicochemical removal of dyes from wastewater: a critical review, Sci. Total Environ., 640–641 (2018) 772–797.
[6] J. Deng, S. Feng, X. Ma, C. Tan, H. Wang, S. Zhou, T. Zhang, J. Li, Heterogeneous degradation of Orange II with peroxymonosulfate activated by ordered mesoporous $MnFe_2O_4$, Sep. Purif. Technol., 167 (2016) 181–189.
[7] K.G. Bastidas G, C.A. Sierra, H.R.Z. Ramirez, Heterogeneous Fenton oxidation of Orange II using iron nanoparticles supported on natural and functionalized fique fiber, J. Environ. Chem. Eng., 6 (2018) 4178–4188.
[8] Y. Chen, P. Deng, P. Xie, R. Shang, Z. Wang, S. Wang, Heat-activated persulfate oxidation of methyl- and ethyl-parabens: effect, kinetics, and mechanism, Chemosphere, 168 (2017) 1628–1636.
[9] J. Ma, H. Li, L. Chi, H. Chen, C. Chen, Changes in activation energy and kinetics of heat-activated persulfate oxidation of phenol in response to changes in pH and temperature, Chemosphere, 189 (2017) 86–93.
[10] R. Xiao, Z. Luo, Z. Wei, S. Luo, R. Spinney, W. Yang, D.D. Dionysiou, Activation of peroxymonosulfate/persulfate by nanomaterials for sulfate radical-based advanced oxidation technologies, Curr. Opin. Chem. Eng., 19 (2018) 51–58.
[11] H. Zhang, Q.Q. Ji, L.D. Lai, G. Yao, B. Lai, Degradation of p-nitrophenol (PNP) in aqueous solution by mFe/Cu-air-PS system, Chin. Chem. Lett., 30 (2019) 1129–1132.
[12] B. Kakavandi, S. Alavi, F. Ghanbari, M. Ahmadi, Bisphenol A degradation by peroxymonosulfate photo-activation coupled with carbon-based cobalt ferrite nanocomposite: performance, upgrading synergy and mechanistic pathway, Chemosphere, 287 (2022) 132024, doi: 10.1016/j.chemosphere.2021.132024.
[13] M. Noorisepehr, B. Kakavandi, A.A. Isari, F. Ghanbari, E. Dehghanifard, N. Ghomi, F. Kamrani, Sulfate radical-based oxidative degradation of acetaminophen over an efficient hybrid system: peroxydisulfate decomposed by ferroferric oxide nanocatalyst anchored on activated carbon and UV light, Sep. Purif. Technol., 250 (2020) 116950, doi: 10.1016/j.seppur.2020.116950.
[14] W.M. Chen, F. Wang, C. He, Q.B. Li, Molecular-level comparison study on microwave irradiation-activated persulfate and hydrogen peroxide processes for the treatment of refractory organics in mature landfill leachate, J. Hazard. Mater., 397 (2020) 122785, doi: 10.1016/j.jhazmat.2020.122785.
[15] J. Wang, S. Wang, Activation of persulfate (PS) and peroxymonosulfate (PMS) and application for the degradation of emerging contaminants, Chem. Eng. J., 334 (2018) 1502–1517.
[16] A.A. Babaei, M. Golshan, B. Kakavandi, A heterogeneous photocatalytic sulfate radical-based oxidation process for efficient degradation of 4-chlorophenol using TiO_2 anchored on Fe oxides@carbon, Process Saf. Environ. Prot., 149 (2021) 35–47.
[17] F. Ghanbari, B. Kakavandi, X.T. Hong, K.Y.A. Lin, Intensified peroxydisulfate/microparticles-zero valent iron process through aeration for degradation of organic pollutants: kinetic studies, mechanism and effect of anions, J. Water Process Eng., 36 (2020) 101321, doi: 10.1016/j.jwpe.2020.101321.
[18] S. Moradi, A.A. Isari, F. Hayati, R.R. Kalantary, B. Kakavandi, Co-implanting of TiO_2 and liquid-phase-delaminated g-C_3N_4 on multi-functional graphene nanobridges for enhancing photocatalytic degradation of acetaminophen, Chem. Eng. J., 414 (2021) 128618, doi: 10.1016/j.cej.2021.128618.
[19] Y. Lee, S. Lee, M.C. Cui, J. Kim, J.J. Ma, Z.C. Han, J. Khim, Improving sono-activated persulfate oxidation using mechanical mixing in a 35-kHz ultrasonic reactor: persulfate activation mechanism and its application, Ultrason. Sonochem., 72 (2021) 105412, doi: 10.1016/j.ultsonch.2020.105412.
[20] S. Nimai, H. Zhang, Z. Wu, N.W. Li, B. Lai, Efficient degradation of sulfamethoxazole by acetylene black activated peroxydisulfate, Chin. Chem. Lett., 31 (2020) 2657–2660.
[21] S.S. Rezaei, B. Kakavandi, M. Noorisepehr, A.A. Isari, S. Zabih, P. Bashardoust, Photocatalytic oxidation of tetracycline by magnetic carbon-supported TiO_2 nanoparticles catalyzed peroxydisulfate: performance, synergy and reaction mechanism studies, Sep. Purif. Technol., 258 (2021) 117936, doi: 10.1016/j.seppur.2020.117936.
[22] Q. Wang, B. Wang, Y. Ma, S. Xing, Enhanced superoxide radical production for ofloxacin removal via persulfate activation with Cu-Fe oxide, Chem. Eng. J., 354 (2018) 473–480.
[23] F. Ghanbari, M. Moradi, Application of peroxymonosulfate and its activation methods for degradation of environmental organic pollutants: review, Chem. Eng. J., 310 (2017) 41–62.
[24] J. Ma, Y. Liu, X. Jin, J. Bai, Catalytic degradation of 4-chlorophenol by persulfate activated with magnetic $CuFe_2O_4$-Fe_3O_4 composite, Desal. Water Treat., 125 (2018) 61–67.
[25] J. Li, Y. Ren, F.Z. Ji, B. Lai, Heterogeneous catalytic oxidation for the degradation of p-nitrophenol in aqueous solution by persulfate activated with $CuFe_2O_4$ magnetic nanoparticles, Chem. Eng. J., 324 (2017) 63–73.
[26] L. Chen, T. Luo, S.J. Yang, J. Xu, Z.Z. Liu, F. Wu, Efficient metoprolol degradation by heterogeneous copper ferrite/sulfite reaction, Environ. Chem. Lett., 16 (2018) 599–603.
[27] J. Kong, R.B. Li, F.L. Wang, P. Chen, H.J. Liu, G.G. Liu, W.Y. Lv, Sulfate radical-induced transformation of trimethoprim with $CuFe_2O_4$/MWCNTs as a heterogeneous catalyst of peroxymonosulfate mechanisms and reaction pathways, RSC Adv., 8 (2018) 24787–24795.
[28] Y. Zhang, Q. Zhang, Z. Dong, L. Wu, J. Hong, Structurally modified $CuFe_2O_4$/persulfate process for acetaminophen scavenging: high efficiency with low catalyst addition, J. Chem. Technol. Biotechnol., 94 (2019) 785–794.
[29] M. Tang, F. Xia, C. Gao, H. Qiu, Preparation of magnetically recyclable $CuFe_2O_4$/RGO for catalytic hydrolysis of sodium borohydride, Int. J. Hydrogen Energy, 41(2016) 13058–13068.
[30] D. Ouyang, J. Yan, L. Qian, Y. Chen, L. Han, A. Su, W. Zhang, H. Ni, M. Chen, Degradation of 1,4-dioxane by biochar supported nano magnetite particles activating persulfate, Chemosphere, 184 (2017) 609–617.
[31] H. Li, Y.F. Qiu, X.L. Wang, J. Yang, Y.J. Yu, Y.Q. Chen, Y.D. Liu, Biochar supported Ni/Fe bimetallic nanoparticles to remove 1,1,1-trichloroethane under various reaction conditions, Chemosphere, 169 (2016) 534–541.
[32] H. Lyu, J. Tang, Y. Huang, L. Gai, E.Y. Zeng, K. Liber, Y. Gong, Removal of hexavalent chromium from aqueous solutions by a novel biochar supported nanoscale iron sulfide composite, Chem. Eng. J., 322 (2017) 516–524.

[33] S. Wang, C. Zhao, R. Shan, Y. Wang, H. Yuan, A novel peat biochar supported catalyst for the transesterification reaction, Energy Convers. Manage., 139 (2017) 89–96.
[34] Y. Wu, J. Guo, Y. Han, J. Zhu, L. Zhou, Y. Lan, Insights into the mechanism of persulfate activated by rice straw biochar for the degradation of aniline, Chemosphere, 200 (2018) 373–379.
[35] R. Yin, W. Guo, H. Wang, J. Du, Q. Wu, J.-S. Chang, N. Ren, Singlet oxygen-dominated peroxydisulfate activation by sludge-derived biochar for sulfamethoxazole degradation through a nonradical oxidation pathway: performance and mechanism, Chem. Eng. J., 357 (2019) 589–599.
[36] S.F. Jiang, L.L. Ling, W.J. Chen, W.J. Liu, D.C. Li, H. Jiang, High efficient removal of bisphenol A in a peroxymonosulfate/iron functionalized biochar system: mechanistic elucidation and quantification of the contributors, Chem. Eng. J., 359 (2019) 572–583.
[37] H. Luo, Q. Lin, X. Zhang, Z. Huang, S. Liu, J. Jiang, R. Xiao, X. Liao, New insights into the formation and transformation of active species in nZVI/BC activated persulfate in alkaline solutions, Chem. Eng. J., 359 (2019) 1215–1223.
[38] Y. Feng, D. Wu, Y. Deng, T. Zhang, K. Shih, Sulfate radical-mediated degradation of sulfadiazine by $CuFeO_2$ rhombohedral crystal-catalyzed peroxymonosulfate: synergistic effects and mechanisms, Environ. Sci. Technol., 50 (2016) 3119–3127.
[39] Y. Yao, F. Lu, Y. Zhu, F. Wei, X. Liu, C. Lian, S. Wang, Magnetic core-shell $CuFe_2O_4@C_3N_4$ hybrids for visible light photocatalysis of Orange II, J. Hazard. Mater., 297 (2015) 224–233.
[40] J. Zhao, X. Chen, L. Bao, Z. Bao, Y. He, Y. Zhang, J. Li, Correlation between microbial diversity and toxicity of sludge treating synthetic wastewater containing 4-chlorophenol in sequencing batch reactors, Chemosphere, 153 (2016) 138–145.
[41] J.L. Liu, X.M. Li, Q. Yang, D.B. Wang, Y. Wu, Z. Chen, X.D. Huang, Z.J. Pi, W.J. Du, Z.L. Guan, The biochar-supported iron-copper bimetallic composite activating oxygen system for simultaneous adsorption and degradation of tetracycline, Chem. Eng. J., 402 (2020) 126039, doi: 10.1016/j.cej.2020.126039.
[42] Y. Xu, J. Ai, H. Zhang, The mechanism of degradation of Bisphenol A using the magnetically separable $CuFe_2O_4$/peroxymonosulfate heterogeneous oxidation process, J. Hazard. Mater., 309 (2016) 87–96.
[43] T. Wang, Z.Y. Wang, P.L. Wang, Y.Y. Tang, An integration of photo-Fenton and membrane process for water treatment by a PVDF@$CuFe_2O_4$ catalytic membrane, J. Membr. Sci., 572 (2019) 419–427.
[44] H. Zheng, J. Bao, Y. Huang, L. Xiang, Faheem, B. Ren, J. Du, M.N. Nadagouda, D.D. Dionysiou, Efficient degradation of atrazine with porous sulfurized Fe_2O_3 as catalyst for peroxymonosulfate activation, Appl. Catal., 259 (2019) 118056, doi: 10.1016/j.apcatb.2019.118056.
[45] Y. Qiao, J. Wu, Y. Xu, Z. Fang, L. Zheng, W. Cheng, E.P. Tsang, J. Fang, D. Zhao, Remediation of cadmium in soil by biochar-supported iron phosphate nanoparticles, Ecol. Eng., 106 (2017) 515–522.
[46] H. Dong, C. Zhang, K. Hou, Y. Cheng, J. Deng, Z. Jiang, L. Tang, G. Zeng, Removal of trichloroethylene by biochar supported nanoscale zero-valent iron in aqueous solution, Sep. Purif. Technol., 188 (2017) 188–196.
[47] T.J. Al-Musawi, N. Mengelizadeh, K. Sathishkumar, S. Mohebi, D. Balarak, Preparation of $CuFe_2O_4$/montmorillonite nanocomposite and explaining its performance in the sonophotocatalytic degradation process for ciprofloxacin, J. Colloid Interface Sci., 45 (2021) 100532, doi: 10.1016/j.colcom.2021.100532.
[48] F.Z. Qin, Y.J. Peng, G. Song, Q.X. Fang, R.Z. Wang, C. Zhang, G.M. Zeng, D.L. Huang, C. Lai, Y.Y. Zhou, X.F. Tan, M. Cheng, S.Y. Liu, Degradation of sulfamethazine by biochar-supported bimetallic oxide persulfate system in natural water: performance and reaction mechanism, J. Hazard. Mater., 398 (2020) 122816, doi: 10.1016/j.jhazmat.2020.122816.
[49] X.J. Li, F.Z. Liao, L.M. Ye, L.Z. Yeh. Controlled pyrolysis of MIL-88A to prepare iron carbon composites for synergistic persulfate oxidation of phenol: catalytic performance and mechanism, J. Hazard. Mater., 398 (2020) 122938, doi: 10.1016/j.jhazmat.2020.122938.
[50] Y. Ren, N. Li, J. Feng, T. Luan, Q. Wen, Z. Li, M. Zhang, Adsorption of Pb(II) and Cu(II) from aqueous solution on magnetic porous ferrospinel $MnFe_2O_4$, J. Colloid Interface Sci., 367 (2012) 415–421.
[51] X. Wu, F. Xia, Z. Nan, Facile synthesis of double-mesoporous-shelled hollow spheres of Cu-$CuFe_2O_4/SiO_2$ composite as excellent Fenton catalyst, Mater. Chem. Phys., 242 (2020) 122490, doi: 10.1016/j.matchemphys.2019.122490.
[52] H. Zhang, Y. Song, L.C. Nengzi, J. Gou, B. Li, X. Cheng, Activation of persulfate by a novel magnetic $CuFe_2O_4/Bi_2O_3$ composite for lomefloxacin degradation, Chem. Eng. J., 379 (2020) 122362, doi: 10.1016/j.cej.2019.122362.
[53] B. Saravanakumar, S.P. Ramachandran, G. Ravi, V. Ganesh, R.K. Guduru, R. Yuvakkumar, Electrochemical performances of monodispersed spherical $CuFe_2O_4$ nanoparticles for pseudocapacitive applications, Vacuum, 168 (2019) 108798, doi: 10.1016/j.vacuum.2019.108798.
[54] X. Ma, R. Hao, Z. Wang, P. Xu, Y. Luo, Y. Zhao, Nanoscale $CuFe_2O_4$ monodispersedly anchored on reduced graphene oxide as excellent peroxydisulfate catalyst for removal of gaseous elemental mercury, Chem. Eng. J., 401 (2020) 126101, doi: 10.1016/j.cej.2020.126101.
[55] A. Lykoudi, Z. Frontistis, J. Vakros, I.D. Manariotis, D. Mantzavinos, Degradation of sulfamethoxazole with persulfate using spent coffee grounds biochar as activator, J. Environ. Manage., 271 (2020) 111022, doi: doi: 10.1016/j.jenvman.2020.111022.
[56] Y.L. Zhao, X.Z. Yuan, X.D. Li, L.B. Jiang, H. Wang, Burgeoning prospects of biochar and its composite in persulfate-advanced oxidation process, J. Hazard. Mater., 409 (2021) 124893, doi: 10.1016/j.jhazmat.2020.124893.
[57] J. Wang, J.Y. Cai, S.Q. Wang, X.Q. Zhou, X.T. Ding, J. Ali, L. Zheng, S.L. Wang, L. Yang, S. Xi, M.J. Wang, Z.Q. Chen, Biochar-based activation of peroxide: multivariate-controlled performance, modulatory surface reactive sites and tunable oxidative species, Chem. Eng. J., 428 (2022) 131233, doi: 10.1016/j.cej.2021.131233.
[58] D. Ma, Y. Yang, B. Liu, G. Xie, C. Chen, N. Ren, D. Xing, Zero-valent iron and biochar composite with high specific surface area via K_2FeO_4 fabrication enhances sulfadiazine removal by persulfate activation, Chem. Eng. J., 408 (2021) 127992, doi: 10.1016/j.cej.2020.127992.
[59] X. Ren, J. Wang, J. Yu, B. Song, H. Feng, M. Shen, H. Zhang, J. Zou, G. Zeng, L. Tang, J. Wang, Waste valorization: transforming the fishbone biowaste into biochar as an efficient persulfate catalyst for degradation of organic pollutant, J. Cleaner Prod., 291 (2021) 125225, doi: 10.1016/j.jclepro.2020.125225.
[60] J. Ding, W. Xu, S. Liu, Y. Liu, X. Tan, X. Li, Z. Li, P. Zhang, L. Du, M. Li, Activation of persulfate by nanoscale zero-valent iron loaded porous graphitized biochar for the removal of 17-β-estradiol: synthesis, performance and mechanism, J. Colloid Interface Sci., 588 (2021) 776–786.
[61] H.Z. Wang, W.Q. Guo, R.L. Yin, J.S. Du, Q.L. Wu, H.C. Luo, B.H. Liu, F. Sseguya, N.Q. Ren, Biochar-induced Fe(III) reduction for persulfate activation in sulfamethoxazole degradation: insight into the electron transfer, radical oxidation and degradation pathways, Chem. Eng. J., 362 (2019) 561–569.
[62] Q. Ji, X. Cheng, Y. Wu, W. Xiang, H. He, Z. Xu, C. Xu, C. Qi, S. Li, L. Zhang, S. Yang, Visible light absorption by perylene diimide for synergistic persulfate activation towards efficient photodegradation of bisphenol A, Appl. Catal., B, 282 (2021) 119579, doi: 10.1016/j.apcatb.2020.119579.
[63] H. Huang, T. Guo, K. Wang, Y. Li, G. Zhang, Efficient activation of persulfate by a magnetic recyclable rape straw biochar catalyst for the degradation of tetracycline hydrochloride in water, Sci. Total Environ., 758 (2021) 143957, doi: 10.1016/j.scitotenv.2020.143957.
[64] Y. Wang, C. Y. Gao, Y.Z. Zhang, M.K.H. Leung, J.W. Liu, S.Z. Huang, G.L. Liu, J.F. Li, H.Z. Zhao, Bimetal-organic framework derived CoFe/NC porous hybrid nanorods as high-performance persulfate activators for bisphenol a

degradation, Chem. Eng. J., 421 (2021) 127800, doi: 10.1016/j.cej.2020.127800.
[65] B. Niu, N. Wang, Y. Chen, M. Yu, Z. Hou, Z. Li, Y. Zheng, Tourmaline synergized with persulfate for degradation of sulfadiazine: Influencing parameters and reaction mechanism, Sep. Purif. Technol. 257 (2021) 117893, doi: 10.1016/j.seppur.2020.117893.
[66] Z.M. He, W.D. Zheng, M.X. Li, W.B. Liu, Y.K. Zhang, Y.B. Wang, Fe2P/biocarbon composite derived from a phosphorus-containing biomass for levofloxacin removal through peroxymonosulfate activation, Chem. Eng. J., 427 (2022) 130928, doi: 10.1016/j.cej.2021.130928.
[67] R. El Asmar, A. Baalbaki, Z. Abou Khalil, S. Naim, A. Bejjani, A. Ghauch, Iron-based metal organic framework MIL-88-A for the degradation of naproxen in water through persulfate activation, Chem. Eng. J., 405 (2021) 126701, doi: 10.1016/j.cej.2020.126701.
[68] C.Q. Gao, W. Yu, Y.C. Zhu, M. Wang, Z.Z. Tang, L. Du, M.Y. Hu, L. Fang, X. Xiao, Preparation of porous silicate supported micro-nano zero-valent iron from copper slag and used as persulfate activator for removing organic contaminants, Sci. Total Environ., 754 (2021) 142131, doi: 10.1016/j.scitotenv.2020.142131.
[69] H. Liu, Y. Liu, L. Tang, J. Wang, J. Yu, H. Zhang, M. Yu, J. Zou, Q. Xie, Egg shell biochar-based green catalysts for the removal of organic pollutants by activating persulfate, Sci. Total Environ., 745 (2020) 141095, doi: 10.1016/j.scitotenv.2020.141095.
[70] S. Chen, L. Ma, Y. Du, W. Zhan, T.C. Zhang, D. Du, Highly efficient degradation of rhodamine B by carbon nanotubes-activated persulfate, Sep. Purif. Technol., 256 (2021) 117788, doi: 10.1016/j.seppur.2020.117788.
[71] Y. Wan, J. Wan, J.R. Zhao, Y. Wang, T. Luo, S. Yang, Y. Liu, Facile preparation of iron oxide doped Fe-MOFs-MW as robust peroxydisulfate catalyst for emerging pollutants degradation, Chemosphere, 254 (2020) 126798, doi: 10.1016/j.chemosphere.2020.126798.
[72] Y. Zhang, Y. Chen, Z.W. Kang, X. Gao, X. Zeng, M. Liu, D.P. Yang, Waste eggshell membrane-assisted synthesis of magnetic $CuFe_2O_4$ nanomaterials with multifunctional properties (adsorptive, catalytic, antibacterial) for water remediation, Colloids Surf., A, 612 (2021) 125874.
[73] B. Wang, Y.N. Li, L. Wang, Metal-free activation of persulfates by corn stalk biochar for the degradation of antibiotic norfloxacin: activation factors and degradation mechanism, Chemosphere, 237 (2019) 124454, doi: 10.1016/j.chemosphere.2019.124454.
[74] P.C. Guo, H.B. Qiu, C.W. Yang, X. Zhang, X.Y. Shao, Y.L. Lai, G.P. Sheng, Highly efficient removal and detoxification of phenolic compounds using persulfate activated by MnO_x@OMC: synergistic mechanism and kinetic analysis, J. Hazard. Mater., 402 (2021) 123846, doi: 10.1016/j.jhazmat.2020.123846.
[75] X. Yu, J. Sun, G. Li, Y. Huang, Y. Li, D. Xia, F. Jiang, Integration of $SO_4^{\bullet-}$-based AOP mediated by reusable iron particles and a sulfidogenic process to degrade and detoxify Orange II, Water Res., 174 (2020) 115622, doi: 10.1016/j.watres.2020.115622.

Supplementary information

Table S1
Specific surface area and pore volume of catalysts

Catalyst	BET surface area (m^2/g)	Total pore volume (mL/g)	Micropore volume (mL/g)	Average pore diameter (nm)
BC	29.46	91.80	10.41	12.46
$CuFe_2O_4$	109.72	139.98	37.61	5.21
CuFe/BC	93.93	132.98	35.95	5.66

Table S2
Reaction rate constants and their correlation coefficients under different operating conditions

No.	CuFe/BC (g/L)	PS (mmol/L)	pH_0	C_0 (mg/L)	BC (g/L)	Fe_2O_3 (g/L)	$CuFe_2O_4$ (g/L)	NO_3^- (mmol/L)	PO_4^{3-} (mmol/L)	Cl^- (mmol/L)	SO_4^{2-} (mmol/L)	TBA (mmol/L)	EtOH (mmol/L)	NaN_3 (mmol/L)	k_1	R^2
1	1	10	6	50											0.106	0.930
2		10	6	50	1										0.013	0.975
3		10	6	50		0.7									0.022	0.980
4		10	6	50			0.7								0.029	0.991
5	0.5	10	6	50											0.018	0.972
6	0.8	10	6	50											0.053	0.987
7	1.2	10	6	50											0.103	0.998
8	1	4	6	50											0.044	0.996
9	1	6	6	50											0.053	0.981
10	1	8	6	50											0.078	0.970
11	1	12	6	50											0.104	0.997
12	1	10	3	50											0.098	0.966
13	1	10	5	50											0.098	0.992
14	1	10	7	50											0.090	0.958
15	1	10	9	50											0.091	0.996
16	1	10	6	50				10							0.063	0.970
17	1	10	6	50					10						0.011	0.997
18	1	10	6	50						10					0.069	0.937
19	1	10	6	50							10				0.054	0.966
20	1	10	6	50								5			0.044	0.997
21	1	10	6	50									5		0.030	0.998
22	1	10	6	50										5	0.067	0.998

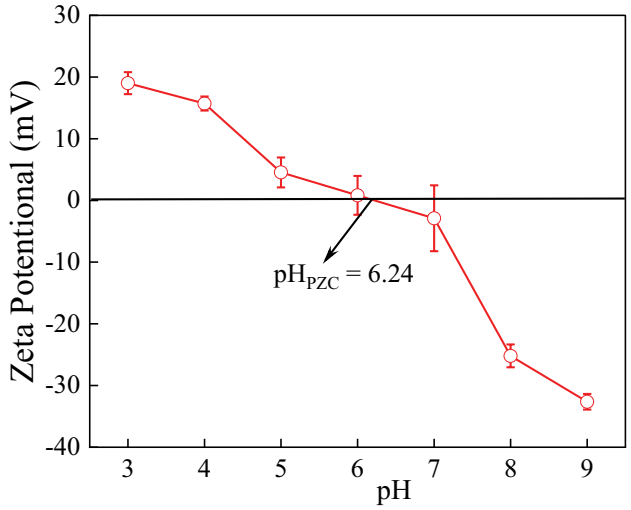

Fig. S1. Zeta potential of CuFe/BC composites as a function of pH.

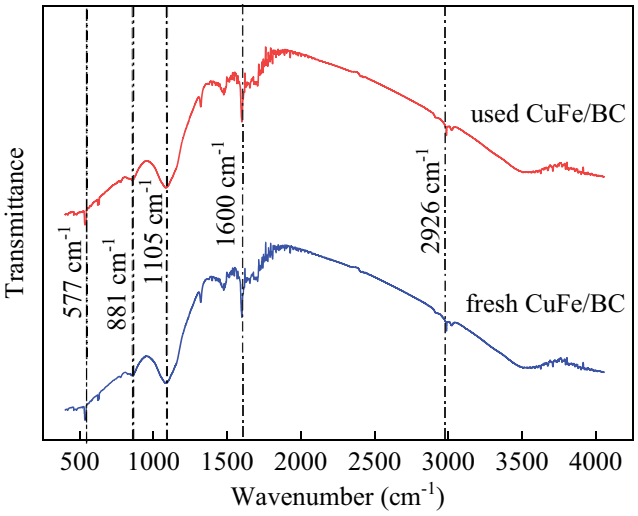

Fig. S3. FTIR spectra of fresh CuFe/BC and used CuFe/BC.

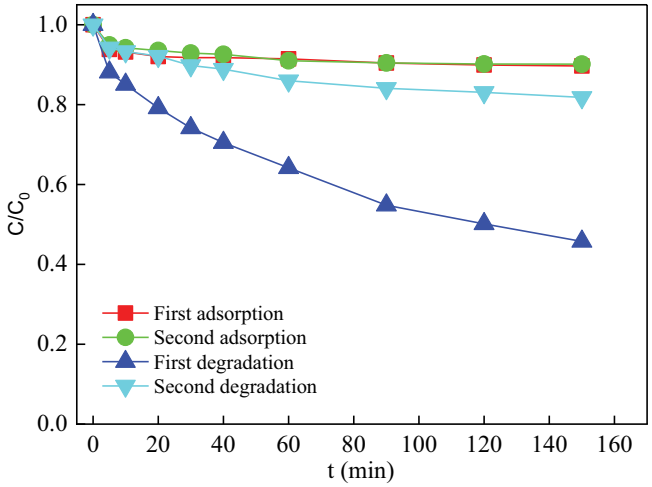

Fig. S2. The reusability and the adsorption of BC for AOII C_0 = 50 mg/L, pH = 6, PS = 10 mM, BC = 1 g/L.

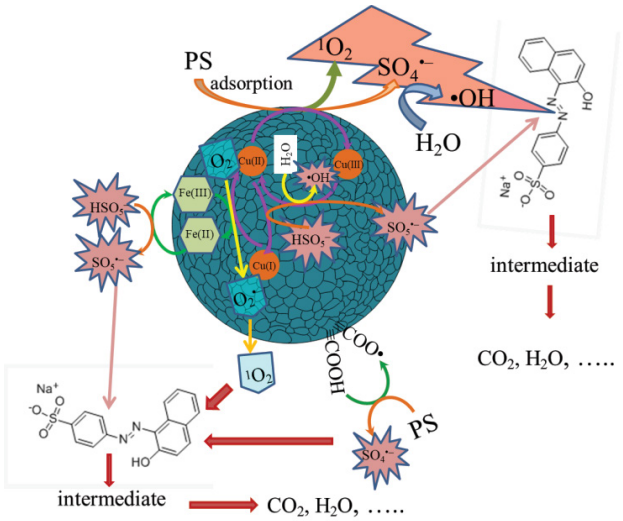

Fig. S4. Proposed mechanism of PS activation for AOII degradation on CuFe/BC.